nature materials

ARTICLES

https://doi.org/10.1038/s41563-020-0638-3

Check for updates

Enhancement-mode ion-based transistor as a comprehensive interface and real-time processing unit for in vivo electrophysiology

Claudia Cea[1,4], George D. Spyropoulos[1,4], Patricia Jastrzebska-Perfect[1], José J. Ferrero[2], Jennifer N. Gelinas[2,3]✉ and Dion Khodagholy[1]✉

Bioelectronic devices must be fast and sensitive to interact with the rapid, low-amplitude signals generated by neural tissue. They should also be biocompatible and soft, and should exhibit long-term stability in physiologic environments. Here, we develop an enhancement-mode, internal ion-gated organic electrochemical transistor (e-IGT) based on a reversible redox reaction and hydrated ion reservoirs within the conducting polymer channel, which enable long-term stable operation and shortened ion transit time. E-IGT transient responses depend on hole rather than ion mobility, and combine with high transconductance to result in a gain–bandwidth product that is several orders of magnitude above that of other ion-based transistors. We used these transistors to acquire a wide range of electrophysiological signals, including in vivo recording of neural action potentials, and to create soft, biocompatible, long-term implantable neural processing units for the real-time detection of epileptic discharges. E-IGTs offer a safe, reliable and high-performance building block for chronically implanted bioelectronics, with a spatiotemporal resolution at the scale of individual neurons.

Bioelectronic devices capable of safely capturing, amplifying, processing and stimulating neurons are required to understand and modulate brain function[1,2]. Organic mixed-conducting materials that transduce ions to electrons can most effectively convert ionic neural signals to those suitable for input to electronics[3]. Transistors are required for complex circuit operations, but a lack of both suitable materials and transistor architectures limits the use of ion-based devices in applications that require stable interactions with neural networks. We previously developed internal ion-gated organic electrochemical transistors (IGTs) to address this challenge[4]. IGTs maintain hydrated ion reservoirs within a conducting polymer channel, reducing the transit time of ions participating in the de-doping process and enabling high operating speed. They are individually addressable due to the incorporation of an ion membrane between the channel and gate electrode. However, these IGTs function only in depletion mode (d-IGTs, normally ON). Because most integrated circuits are currently designed based on enhancement-mode (normally OFF) transistors, enhancement-mode IGTs (e-IGTs) would permit seamless integration with pre-existing designs. In addition, having equally high-performance enhancement- and depletion-mode devices would enable unique integrated circuit design opportunities to diversify the functions executed by bioelectronic devices.

Enhancement-mode operation is employed across different transistor architectures. Silicon field effect transistors (Si-FETs) typically operate in enhancement mode due to the increased performance and ease of fabrication compared with their depletion-mode counterparts. However, Si-FETs are rigid and require strong encapsulation in physiologic environments because ion diffusion damages the silicon components[5,6]. These properties also restrict the abiotic/biotic coupling to a capacitive interaction between the surface of the gate material and electrolyte. Channels based on nanoparticles of zinc oxide and organic semiconductors are used in electrolyte-gated enhancement-mode transistors to enable direct coupling of ions in the electrolyte with the channel through a large double-electric-layer capacitance[7–11]. Organic electrochemical transistors (OECTs) demonstrate volumetric capacitance because hydrophilic conducting polymer channels undergo bulk redox reactions[12]. In contrast with depletion-mode OECTs composed of poly(2,3-dihydrothieno-1,4-dioxin)-poly(styrenesulfonate) (PEDOT:PSS), enhancement-mode OECTs are often unstable and based on non-biocompatible solvents[13–15]. Furthermore, the transient response of these transistors is defined by the 'time of flight' of ions through the gate–electrolyte–channel circuit[16]. Operation speeds are therefore dictated by ion mobility and cannot be improved by enhancing the electronic performance of the channel material[17]. Although such speeds may suffice for limited sensing applications, they are inadequate for the creation of advanced integrated bioelectronics[18].

Here, we developed an easily synthesizable, biocompatible composite of PEDOT:PSS and polyethylenimine (PEI) to create e-IGTs. E-IGTs have high transconductance, exhibit volumetric capacitance and can be stably operated over extended periods of time. Temporal responses of e-IGTs are best described by hole mobility due to the shortened ionic transit time enabled by hydrated ion reservoirs within the e-IGT channel. E-IGTs possess both high transconductance and speed, resulting in a measure of gain–bandwidth product several orders of magnitude above that of other ion-based transistors. We deployed e-IGTs in a wide range of neurophysiological applications, including acquisition of action potentials from individual neurons and real-time detection of epileptic discharges in vivo. E-IGTs are optimal for the creation of integrated circuits in bioelectronic devices.

[1]Department of Electrical Engineering, Columbia University, New York, NY, USA. [2]Institute for Genomic Medicine, Columbia University Medical Center, New York, NY, USA. [3]Department of Neurology, Columbia University Medical Center, New York, NY, USA. [4]These authors contributed equally: Claudia Cea, George D. Spyropoulos. ✉e-mail: jng2146@cumc.columbia.edu; dk2955@columbia.edu

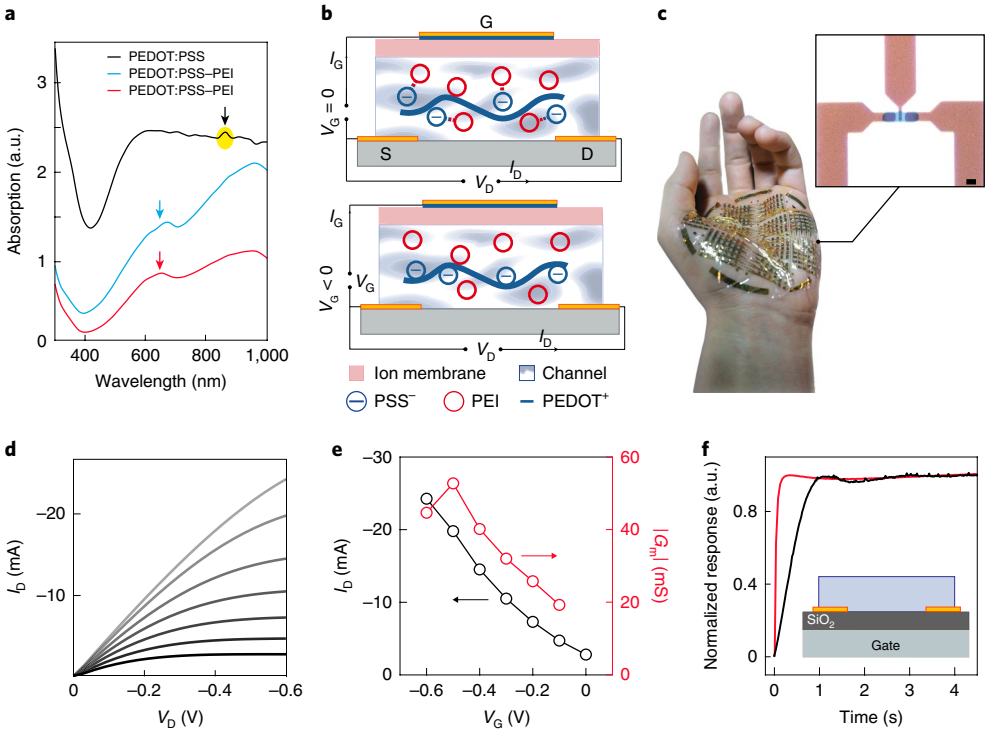

Fig. 1 | Operating mechanism, structure, and steady-state characteristics of an e-IGT. a, Representative absorption spectra of PEDOT:PSS and PEDOT:PSS treated with D-sorbitol and PEI ($n=4$; see Supplementary Fig. 1). Black arrow shows peak indicating the existence of polarons in untreated PEDOT:PSS that is reduced when PEI is added. Light blue (PEDOT:PSS–PEI) and red (diluted PEDOT:PSS–PEI in sorbitol) arrows indicate the emergence of a 600 nm peak. **b**, Schematic illustration of e-IGT cross-section and wiring diagram for device operation. Protonated PEI (red) bonds with PSS^- (blue), de-doping the PEDOT chain ($V_G=0$ V, top). Under a negative applied gate voltage ($V_G<0$ V, bottom), PEI^+ is deprotonated and releases PSS, which then recombines with PEDOT and increases channel conductivity. D-sorbitol creates hydrated ion reservoirs within the channel. PEDOT-rich regions are shown in light blue and PSS lamellas in white (G, S and D denote gate, source and drain terminals, respectively). **c**, Optical micrograph displaying the top view of an individual e-IGT (top right). Scale bar, 5 µm. Ultra-flexible, ultra-thin e-IGT array conforming to the surface of a human hand (bottom left). **d**, Output characteristics (I_D–V_D) of the e-IGT device (length (L) = 5 µm, width (W) = 500 µm, thickness of PEDOT:PSS = 300 nm) for V_G varying from 0 V (bottom curve) to −0.6 V (top curve) with a step of −0.1 V; colour intensity corresponds to V_G amplitude. **e**, Transfer curve for $V_D=-0.6$ V (black) with corresponding transconductance (red), $G_m^{max}=52.74$ mS. **f**, Normalized response of drain current with respect to gate voltage pulse of a PEDOT:PSS–PEI channel gated through chitosan (red; $V_D=-0.6$ V and V_G varying from 0 V to −0.3 V) versus a PEDOT:PSS–PEI channel gated through a 90 nm thick SiO_2 layer (black; $V_D=-10$ V and V_G varying from 0 V to −20 V). Inset shows schematic cross-sectional illustration of PEDOT:PSS–PEI channel with a SiO_2 ion barrier layer. Channel dimensions for both devices were $L=5$ mm and $W=10$ mm, with a thickness of PEDOT:PSS = 300 nm (representative data from $n=3$ experiments).

The e-IGT channel is composed of PEDOT:PSS, PEI, D-sorbitol and cross-linking additives (see Methods). PEDOT:PSS is a highly stable and versatile conducting polymer that can achieve high conductivities and convert ions to electrons[19]. D-sorbitol is a sugar alcohol that stretches the PEDOT:PSS-rich domains and enhances the electronic conductivity of PEDOT:PSS films[20]. It also facilitates the maintenance and movement of mobile ions within the channel by forming hydrated ion reservoirs[4]. The amine groups of PEI transfer electrons to PEDOT:PSS, reducing it and decreasing the intrinsic conductivity of the channel by several orders of magnitude (Supplementary Fig. 1a)[21–23]. The occurrence of this redox reaction is supported by the decrease in absorption in the near infra-red (due to fewer polarons) and emergence of an absorption peak at 600 nm (associated with a colour change to cobalt blue; Fig. 1a and Supplementary Fig. 1b,c) when PEDOT:PSS and PEI are mixed[24,25]. All materials used in the fabrication of IGTs are biocompatible.

We hypothesized that a reduced-PEDOT:PSS film containing excess PEI and PSS, combined with the ease of ion movement within the channel material, could carry out repeatable and reversible ion-based doping to create an enhancement-mode transistor. During the initial OFF state of the device ($V_G=0$ V), the conducting polymer is in its reduced ($PEDOT^0$) state due to electron transfer from PEI. The now protonated PEI^+ establishes ionic bonds with PSS^- to maintain charge balance. This process is naturally facilitated by the presence of sulfonic acid groups in PSS and the basic nature of PEI (Fig. 1b, top)[23,24]. During the ON state, the application of a negative V_G ($V_G<0$) will compensate the PEI^+ in the channel and release the bonded PSS^-, which then recombines with PEDOT (Fig. 1b, bottom). This formation of $PEDOT^+$:PSS^- increases the channel conduction, providing the mechanism whereby application of a gate voltage modulates the channel current. The embedded hydrated reservoirs established by D-sorbitol within the channel facilitate these ion exchanges and eliminate the need for an external electrolyte to operate the device (Fig. 1b).

To allow independent control of individual transistors, the gate electrode must have efficient ionic, but not electronic, conduction with the transistor channel. We chose chitosan for the transistor's ion membrane due to its biocompatibility, stability and processability[26,27]. The ion membrane additionally must not disrupt the charge balance of the PEDOT:PSS–PEI composite. Alternative biopolymers, such as gelatin, polyvinyl alcohol (PVA) and PVA:PSS, were also able to serve as the ion membrane (Supplementary Fig. 2).

E-IGTs were fabricated using established microfabrication processes (Supplementary Fig. 3a,b) capable of creating large-scale conformable transistors and circuits (Fig. 1c and Supplementary Fig. 3c). The transistor operated in enhancement mode, as an

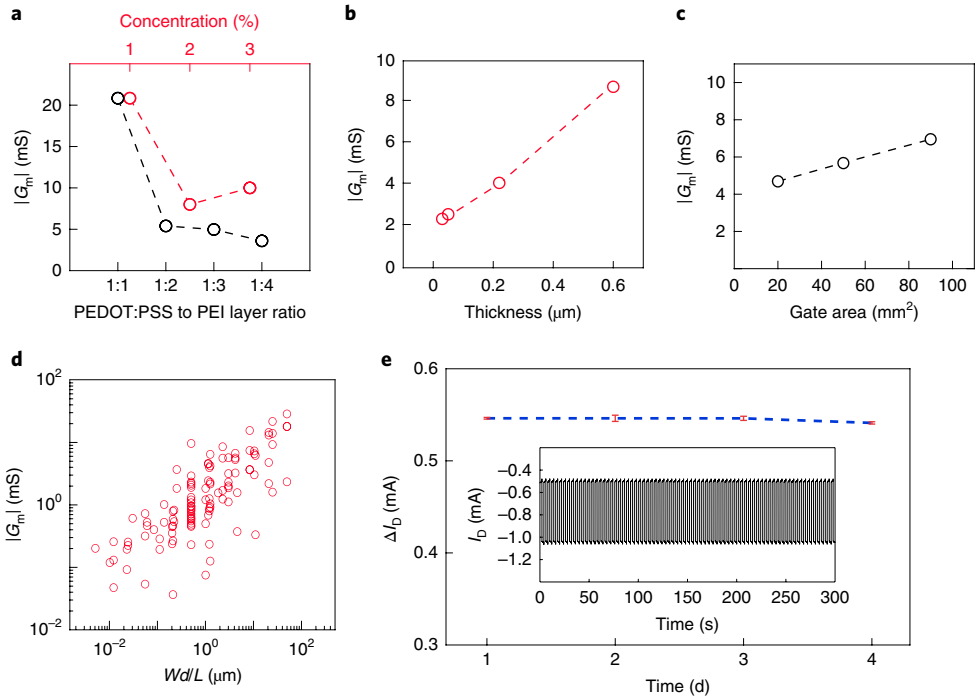

Fig. 2 | PEDOT:PSS–PEI composite creates long-term, stable, volumetric capacitance for the operation of an enhancement-mode transistor. a, Maximum transconductance as a function of PEI solution concentration (top) and PEDOT:PSS to PEI layer ratio (bottom, PEI solution concentration = 1%). Transconductance was calculated based on a transfer curve for $V_D = -0.6$ V and V_G varying from 0 V to −0.6 V ($L = 5$ mm, $W = 10$ mm, representative data from $n = 3$ experiments). **b**, Maximum transconductance increases proportionally with channel thickness. Transconductance was calculated from a transfer curve for $V_D = = -0.6$ V and V_G varying from 0 V to −0.6 V ($L = 5$ mm, $W = 10$ mm, representative data from $n = 3$ experiments). **c**, Maximum transconductance increases proportionally with gate area. Transconductance was estimated from a transfer curve with $V_D = -0.6$ V and V_G varying from 0 V to −0.6 V ($L = 250$ μm, $W = 10$ mm, representative data from $n = 3$ experiments). **d**, Maximum transconductance increases proportionally with channel volume. Transconductance was calculated for a 6 × 6 array of e-IGTs with logarithmically increasing channel length and width (5–500 μm) from a transfer curve with $V_D = -0.6$ V and $V_G = 0$ V to −0.6 V (d denotes channel thickness, $n = 113$ transistors). **e**, Drain-current (I_D) modulation of an e-IGT over a period of four days with pulsed gate voltages ($V_D = -0.4$ V and V_G varying from 0 V to −0.6 V; $W = 500$ μm, $L = 30$ μm, thickness of PEDOT:PSS = 150 nm). Each point represents the average modulation of the transistor under continuous operation for 50 min. Error bars (red) represent the maximum and minimum value for each data point. Inset shows the temporal response of the drain current (I_D) of the e-IGT under continuous operation for 300 s ($n = 3{,}000$ pulses, day 1 = 0.546 mA ± 0.915 μA, day 2 = 0.546 mA ± 3.387 μA, day 3 = 0.546 mA ± 2.250 μA, day 4 = 0.541 mA ± 1.256 μA; mean ± standard deviation).

increase in the negative potential of V_G resulted in a higher drain current (Fig. 1d and Supplementary Fig. 4). We found that e-IGTs achieve high transconductances, exceeding the majority of electrolyte-gated and electrochemical transistors with similar or larger geometries (Fig. 1e and Supplementary Table 2)[4,28–31]. Next, we confirmed that e-IGTs can function in the absence of an external ionic source, such as an electrolyte. We deposited Au-based source and drain electrodes onto a 90 nm thick, thermally grown SiO_2 silicon wafer. The SiO_2 served as an ideal ion barrier, and the channel was formed by spin coating the composite materials in between the source and drain electrodes. It was possible to enhance the drain current by a gate pulse applied through the bulk of the Si, suggesting that the PEDOT:PSS–PEI-based composite is capable of self-doping (Fig. 1f).

We characterized how the amount of excess PEI in the channel affects device function. Higher amounts of excess PEI resulted in a lower OFF-state current, but simultaneously reduced the ON-state current and lowered transconductance (Fig. 2a). The e-IGT transconductance also increased systematically with channel thickness (Fig. 2b). This result implies that the PEI distributed throughout the conducting polymer was able to uniformly reduce the entire channel. Increasing the amount of PEI relative to PEDOT:PSS in the channel also shifted the threshold voltage of the transistor to more negative values, as minimal PEDOT:PSS was available for further de-doping at positive gate voltages. We fabricated an array of e-IGTs with channel length and width that ranged from 5 to 500 μm and found that the transconductance of e-IGTs increased proportionally with respect to gate area and channel volume (Fig. 2c,d). E-IGTs demonstrated stable, constant modulation of drain current in response to a train of gate voltage pulses (both at high V_G pulse amplitude and when biased at maximum transconductance) delivered for four days in physiological conditions (Fig. 2e and Supplementary Fig. 5) and under mechanical stress (Supplementary Fig. 6). The duration of these stability experiments was defined based on requirements for electrophysiology rather than device failure. Excess PEI and PSS in the e-IGT channel enabled stable operation by (1) maintaining protons localized within the channel despite the absence of an ionic barrier between the channel and ion membrane, and (2) preserving the channel in its reduced form without gradual oxidation.

High-speed transistors are required for many neurophysiologic applications, such as recording neural action potentials (complex waveform duration 1–2 ms (ref. [32])) or performing signal processing for responsive neurostimulation[33]. The time constant (τ) for electrochemical transistors and electrolyte-gated FETs is defined by the device geometry and ionic mobility because the transient dynamics of such devices are described using an ionic-based resistor–capacitor (RC) circuit between the gate and channel[16]. We previously showed that maintaining mobile ionic species within the polymeric channel decreases the 'time-of-flight' of ions engaged in the de-doping process by reducing the average travelling distance

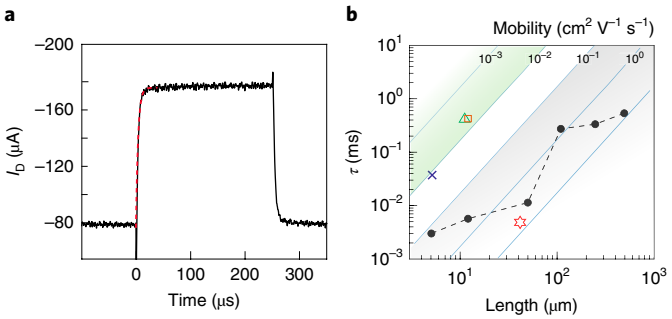

Fig. 3 | High-speed transient response of an e-IGT is a function of hole rather than ion mobility. a, Temporal response of the drain current (I_D) of an e-IGT device with $L = 5\,\mu m$, $W = 5\,\mu m$ (thickness of PEDOT:PSS = 100 nm) biased at $V_D = -0.6\,V$ and $V_G = -0.4\,V$, with pulse amplitude of 0.2 V. Exponential fit of the e-IGT drain current (red) resulted in a time constant of 2.9 μs ($n = 256$ pulses). **b**, Rise time for e-IGTs with different channel lengths (black circles) fall within the theoretical ranges governed by hole mobility (grey shaded area). Blue lines show the theoretical achievable rise time based on the corresponding carrier mobilities ranging from 10^{-3} to 10 $cm^2\,V^{-1}\,s^{-1}$. Rise times of other ion-based transistors (cross[29], triangle[13], rectangle[48]) fall within ranges governed by ion mobility (green shaded area); the poly-Si-based enhancement-mode transistor (star[49]) falls in the hole-mobility regime. Note, $n = 256$ pulses per data point; see Supplementary Fig. 9 and Supplementary Table 1 for device details.

of the ions[4]. An e-IGT with a 5 μm channel length had a rise time of 2.9 μs while maintaining ~1.5 mS transconductance (Fig. 3a and Supplementary Fig. 7). This speed of operation is several orders of magnitude faster than that reported for enhancement-mode ion-based (electrochemical or electrolyte-gated, organic or inorganic) transistors (Supplementary Tables 1–2). To better understand the transient dynamics of the e-IGT, we systematically fabricated devices with various channel lengths and measured the rise time and hole mobility using constant gate voltages and current pulses, respectively (Fig. 3b and Supplementary Figs. 8,9). In contrast with OECTs and electrolyte gated organic field effect transistors (EGOFETs), e-IGT transient responses fall within the range of hole mobility (0.1–10 $cm^2\,V^{-1}\,s^{-1}$)[34–36] rather than ion mobility values (10^{-2}–10^{-4} $cm^2\,V^{-1}\,s^{-1}$)[17] in conducting polymers (Fig. 3b, Supplementary Fig. 10 and Supplementary Table 1). E-IGT architecture can therefore leverage the higher hole mobility of conducting polymers to increase operation speed compared with other organic electrochemical devices where speed is dictated by ion mobility.

However, transistors must have both high speed and high amplification to function effectively in bioelectronic circuits[37,38], and these parameters are often inversely related due to the geometrical design and material composition of the device. To evaluate this trade-off in e-IGTs, we characterized transistor performance based on the ratio of transconductance and rise time as a measure of gain–bandwidth product. E-IGTs performed favourably compared with most organic transistor architectures, and surpassed the majority of enhancement-mode transistors by several orders of magnitude (Fig. 4a, Supplementary Fig. 11 and Supplementary Table 2).

We next investigated the feasibility of using e-IGTs for integrated circuits. A key factor that limits integrated circuit design is cross-talk and current leakage between adjacent transistors. Depletion-mode transistors have a high conductivity in the unbiased channel, necessitating complex patterning processes to eliminate high current leakage between adjacent transistors. This feature often poses a significant fabrication challenge because organic electronic materials are highly sensitive to photolithographic chemicals, which include strong bases and solvents. Although peel-off techniques can enable appropriate patterning in some cases, the deposition layer must be substantially thinner than the peel-off layer, limiting the design and material possibilities[18,39]. In contrast with depletion-mode devices, the low OFF current (high resistance) of the e-IGT in its unbiased state allows for high-resistance paths between adjacent transistors in the absence of any channel patterning (Supplementary Fig. 12). We fabricated digital logic gates (AND, OR gates) that accurately performed the corresponding arithmetic, and exhibited minimal gate leakage current (I_G), confirming that e-IGTs can function as scalable, low-leakage bioelectronic computational modules (Fig. 4b,c).

We designed a series of experiments to evaluate the applicability of e-IGTs to a broad range of electrophysiological measurements, including non-invasive electromyography (EMG) and electrocardiography (ECG) from surface of human skin, as well as chronic intracranial encephalography from the surface of the brain and deeper structures in freely moving rats. We were able to create e-IGT-based devices with various form factors to accommodate the different mechanical and electrical requirements of each application due to the e-IGT's versatile architecture and fabrication process. Specifically, the devices adequately surveyed the entire electrophysiological frequency spectrum (0.1–10^4 Hz) with an appropriate signal-to-noise ratio (SNR) for each signal's amplitude (Fig. 5a).

We performed e-IGT-based EMG and ECG, recording from the skin over the right biceps muscle and left chest, respectively, of healthy volunteers ($n = 3$). E-IGTs required minimal force to maintain contact with the skin due to their lightweight and conformable design (Fig. 5b). The e-IGT was placed in a common-source configuration with an adhesive electrode on the left forearm serving as a ground for measurement with a source measure unit in both cases (Fig. 5c). We recorded low noise, high SNR (see Supplementary Fig. 13) muscle compound action potentials triggered by voluntary flexion of the biceps muscle (Fig. 5c and Supplementary Fig. 13). ECG recording revealed a typical waveform morphology with well-distinguished QRS complexes, comparable with the signal obtained with commercially available medical electrodes connected to a differential amplifier (Supplementary Fig. 13). These results confirm the ability of the e-IGT to effectively function as a non-invasive electrophysiological transducer.

We next used e-IGTs to perform chronic, invasive brain recording in an animal model. We fabricated two types of devices to mimic the electrode configurations typically employed to record from brain networks: (1) conformable surface arrays of e-IGTs for placement on the cortical surface, and (2) strips with e-IGTs at the tip for insertion into deep cortical layers. A craniotomy was opened over a rat somatosensory cortex, and e-IGT arrays were placed on the cortical surface (Supplementary Fig. 14). The device conformed to the curvilinear surface of the brain and maintained mechanical contact. Two surgical stainless-steel screws implanted in the cerebellum served as the e-IGT gate and the ground for the acquisition amplifier (Supplementary Fig. 14), and recording was initiated using a common-source configuration while the rat was freely moving (Supplementary Fig. 15). We computed the time–frequency spectrogram of e-IGT-based local field potentials (LFPs) recorded two weeks after implantation (Fig. 5d). Characteristic spectral features of non-rapid eye movement (NREM) sleep, rapid eye movement (REM) sleep and wakefulness (WAKE) were identifiable in the recordings. Being able to identify well-characterized behavioural states (such as NREM and REM sleep) confirms the ability of e-IGTs to accurately detect neurophysiologic signals that can be interpreted by neurophysiologists using conventional analysis methods, as is often required during the evaluation of neural signals for clinical purposes. To evaluate the fidelity of the device performance at higher frequencies, we investigated cross-frequency coupling, a phenomenon that is linked to neural computation and information transfer within cortical networks. The cross-frequency coupling demonstrated temporal co-occurrence of brain oscillations

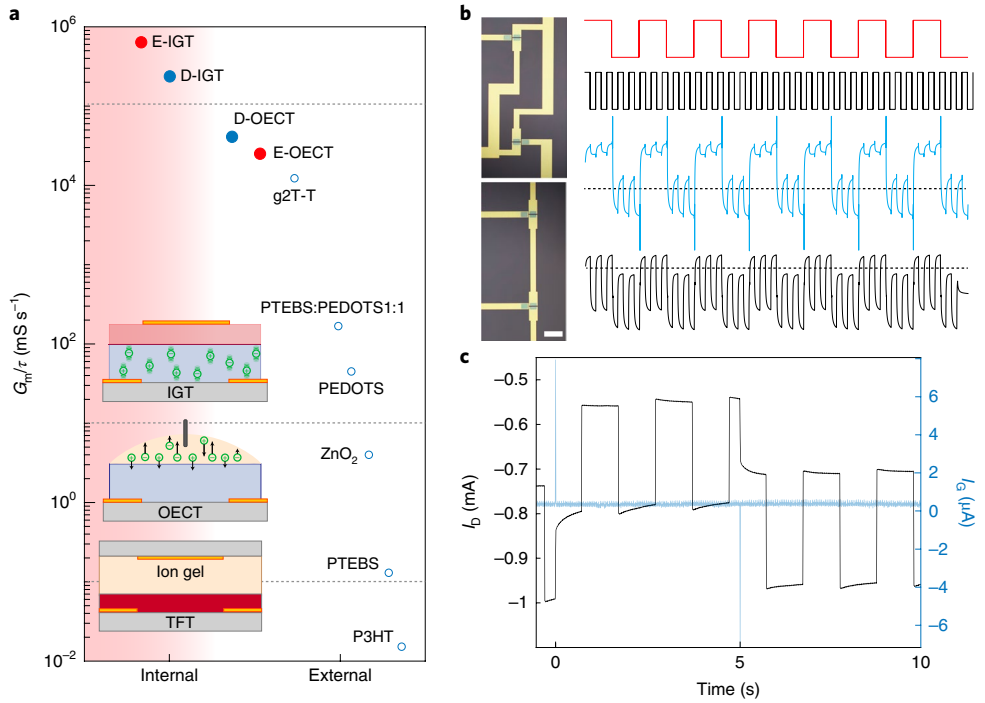

Fig. 4 | E-IGTs have a high gain–bandwidth product and create low-leakage, effective integrated circuits. a, Ratio of transconductance to rise time for different ion-based transistors. Internal mobile ions enable higher G_m/τ compared with external ions supplied by an electrolyte. PEDOT:PSS–PEI based OECTs and IGTs are marked in red (see Supplementary Table 2 for details of all devices). Filled circles denote devices that were fabricated in this study g2T-T denotes poly(2-(3,3′-bis(2-(2-(2-methoxyethoxy)ethoxy)ethoxy)-[2,2′-bithiophen]-5-yl) [3,2-b]thiophene)[14], PTEBS denotes sodium poly(2-(3-thienyl)-ethoxy-4-butylsulfonate), PEDOTS denotes poly(4-(2,3-dihydrothieno-(3,4-b)-(1,4)dioxin-2-yl-methoxy)-1-butanesulfonic acid[50], sodium salt, and P3HT referes to poly(3-hexylthiophene-2,5-diyl)[7]. **b**, Optical micrographs of OR (left, top) and AND (left, bottom) logic gates; scale bar, 150 μm. Input signals (red and black) are the top two traces. Response of AND (light blue) and OR (dark blue) logic gate are the bottom two traces. Dashed lines mark the threshold of high and low logics (representative data from $n=5$ experiments). **c**, E-IGTs perform digital logic with minimal leakage current. The drain current of the e-IGT is shown in black, and the leakage current between the source and gate of an adjacent e-IGT is shown in blue (representative data from $n=5$ experiments).

across a wide frequency spectrum[40]. This analysis replicated the temporal coupling between cortical sleep spindles (10–20 Hz) and both low-gamma (20–30 Hz) and high-gamma (>40 Hz) oscillations previously identified using conventional intracranial electrodes (Fig. 5e)[32,41]. Therefore, e-IGTs are capable of acquiring consistently high-quality LFP data from the cortical surface over a period of two weeks, demonstrating stability in a physiological environment. Post-mortem histological analysis revealed a lack of macroscopic tissue damage, neuronal loss or gliosis in the vicinity of the implanted e-IGTs (Supplementary Fig. 16), supporting device biocompatibility. Although the highly protonated form of PEI may cause cytotoxicity, charge-balanced PEI and its combination with chitosan has been demonstrated to be an effective biocompatible cell scaffolding material[27,42].

Neural spiking provides key insight into the mechanisms of brain function[40,43]. We assessed the capacity of e-IGTs to acquire in vivo neural spiking activity from deep cortical layers, an experimental procedure that is only possible if a neural interface device provides high speed and amplification simultaneously. To ensure an appropriate sampling rate (20 kHz) for the acquisition of action potentials, we converted the drain current of the e-IGT to voltage and digitized it with a 1 kΩ resistor in series between the channel and electrophysiological amplifier (Fig. 5f). E-IGT strips were fabricated onto a narrow, conformable parylene C substrate with an anchor point at the tip to facilitate placement into the cortex (Fig. 5g and Supplementary Fig. 14). This design allowed the device to be wrapped around a 50-μm-wide tungsten microwire to guide device insertion (Fig. 5g). High-pass filtering (>250 Hz) of the neural signals acquired by implanted e-IGTs revealed large amplitude transients suggestive of action potentials (Fig. 5h). Transients detected from individual e-IGTs had a consistent waveform morphology (Fig. 5i, top and left), and autocorrelation of their occurrence times demonstrated a pattern consistent with the physiologic refractory period of a neuron (Fig. 5i, right). These results validate the ability of e-IGTs to record the spiking activity of individual neurons in vivo.

Bioelectronic devices are increasingly required not only to acquire biologic signals, but also to process them in real time[33]. For a subset of patients with epilepsy, responsive neurostimulation approaches with implanted neural interface devices are a promising form of treatment[44]. However, the only components capable of performing these functions at present are silicon-based, non-biocompatible and bulky, and need rigid encapsulation in physiologic environments. We sought to use IGT-based circuitry to create soft, biocompatible, chronically implantable neural processing units. A key function of these responsive neurostimulation devices is the accurate detection of epileptic discharges, which is typically accomplished using bandpass filters or amplitude thresholding[45]. This detection can be challenging due to the variable amplitude of the neural potentials based on the location of the recording electrode with respect to local dipoles and the reference electrode[46,47]. Nonlinear rectification could improve detection by suppressing lower but variable-amplitude non-target signals, but this strategy is not practical to implement using a single transistor type. We combined a d-IGT with an e-IGT to create an IGT-based non-linear rectification circuit (Fig. 6a and Supplementary Fig. 17). This device was used to process signals acquired from the hippocampus of a freely moving epileptic rat (Fig. 6b,c). The IGT-based non-lin-

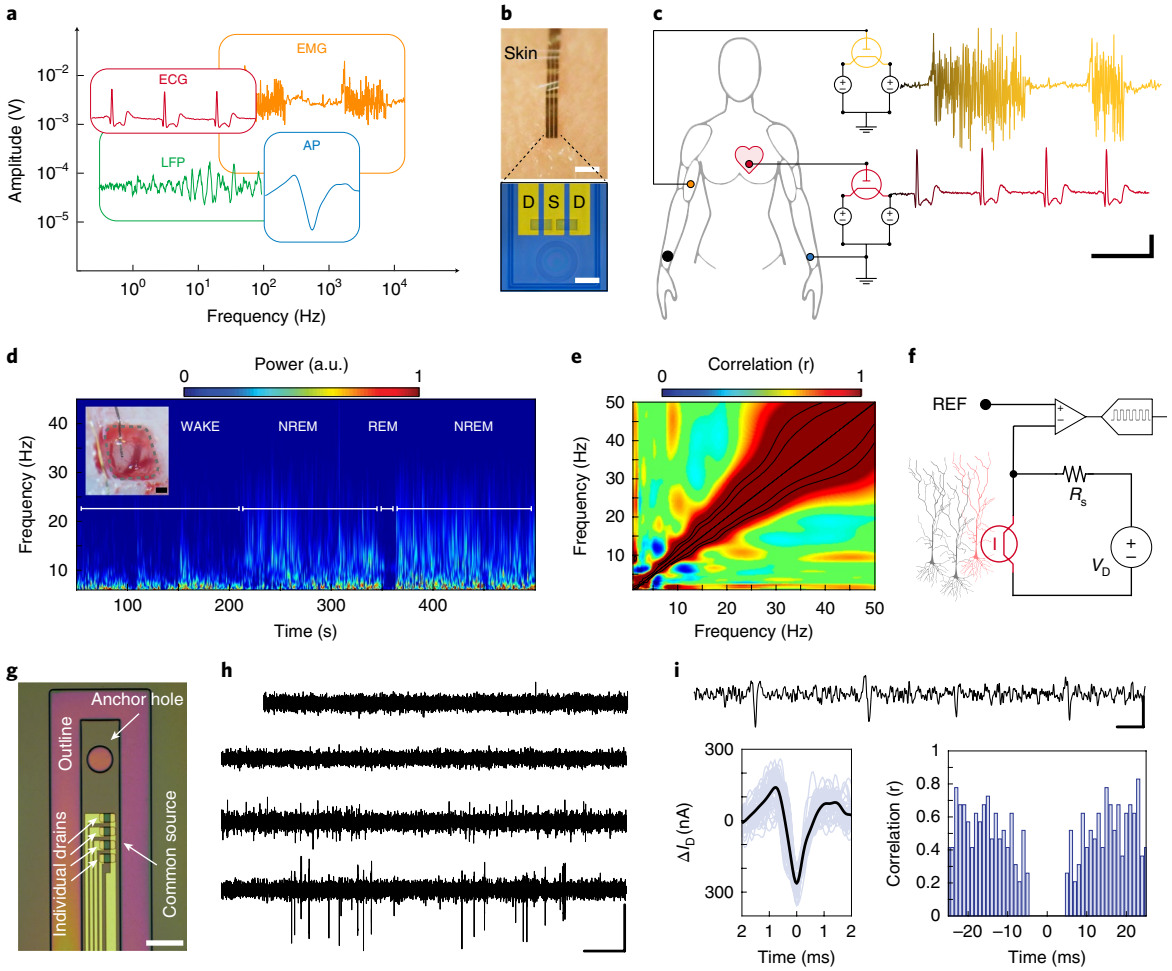

Fig. 5 | E-IGTs enable high-quality electrophysiological signal acquisition across a broad range of frequencies and amplitudes. a, Sample traces of in vivo signals acquired by e-IGTs plotted to reflect the wide span of frequency and amplitude characteristics (representative data from $n=4$ rats). **b**, Micrograph of an e-IGT-based device used for ECG and EMG signal acquisition in contact with human skin (top; scale bar, 150 µm). Optical micrograph of e-IGT devices with two recording channels (bottom; scale bar, 100 µm). The middle source electrode (S) and the two drain electrodes (D) are denoted. **c**, Wiring diagram of EMG and ECG recording using an e-IGT-based device at $V_D=-0.3$ V and $V_G=0$ V. The gate electrode was at the wrist (blue circle), and e-IGTs were placed on the right biceps for EMG recording (yellow circle) and chest for ECG recording (red circle). Sample traces of e-IGT-acquired EMG (yellow) and ECG (red) signals are shown. The black, filled dot on the right hand denotes ground (GND). Scale bar 1 s, 200 µA (see Supplementary Fig. 13; representative data from $n=3$ healthy subjects). **d**, Time–frequency spectrogram of an e-IGT-based chronic LFP recording from a cortical surface with behavioural states marked. Inset shows a photograph of e-IGT-based device placement on rat cortex; scale bar, 500 µm. Warmer colours represent a higher relative power in arbitrary units (representative data from $n=4$ rats). **e**, Comodulogram showing cross-frequency coupling of cortical LFP at spindle, low-gamma and high-gamma frequency bands. Warmer colours represent a higher relative correlation ($P<0.05$ after the Bonferroni–Holm correction for multiple comparisons that were considered statistically significant; representative data from $n=4$ rats). **f**, Wiring diagram of action potential recording using an e-IGT-based implantable device. The drain current was converted to voltage using a series resistor, then digitized using a neurophysiological amplifier ($V_{DS}=-0.4$ V, $V_{GS}=-0.5$ V, while $V_G=0$ V, REF refers to reference voltage). **g**, Optical micrograph of an e-IGT-based device with four transistors for LFP and spike recording. The anchor hole facilitates insertion of the conformable device using a microwire guide into deep layers of rat cortex. The potential generated by neurons serves as the small-signal V_G. Scale bar, 80 µm. **h**, High-pass filtered traces (250–2,500 Hz) from four e-IGTs in deep layers of rat cortex revealing waveforms suggestive of neural action potentials. Scale bar, 300 nA, 500 ms. **i**, High-pass filtered trace showing neural action potential waveforms (top; scale bar, 300 nA, 25 ms). Trigger averaging ($n=50$, spikes are aligned at waveform trough, $t=0$ s) of waveforms demonstrates consistent action potential morphology (black line, bottom left). Autocorrelogram indicative of neural firing refractory period (bottom right, $n=9{,}357$ spikes).

ear rectification circuit accurately detected epileptic discharges (Fig. 6d), with receiver operating characteristics that surpassed traditional amplitude or bandpass filter thresholding methods (Fig. 6e). Therefore, IGTs and their ability to efficiently integrate enhancement- and depletion-mode devices within individual circuits can improve the real-time processing of disease-relevant neurophysiological signals and have the potential to form fully implantable, conformable acquisition and processing units for bioelectronic devices.

We developed enhancement-mode IGTs based on the PEDOT:PSS–PEI composite material. E-IGTs have a high transconductance ($G_m^{max}=52.74$ mS) and exhibit volumetric capacitance. Excess PSS and PEI within the channel composite maintains the PEDOT^0 in its reduced state, allowing long-term reversible de-doping/doping and stable transistor operation over an extended period of time. Transient responses of e-IGT operation are rapid (2.9 µs) and best described by hole mobility. This increase in speed is due to the shortened ionic transit time enabled by hydrated ion

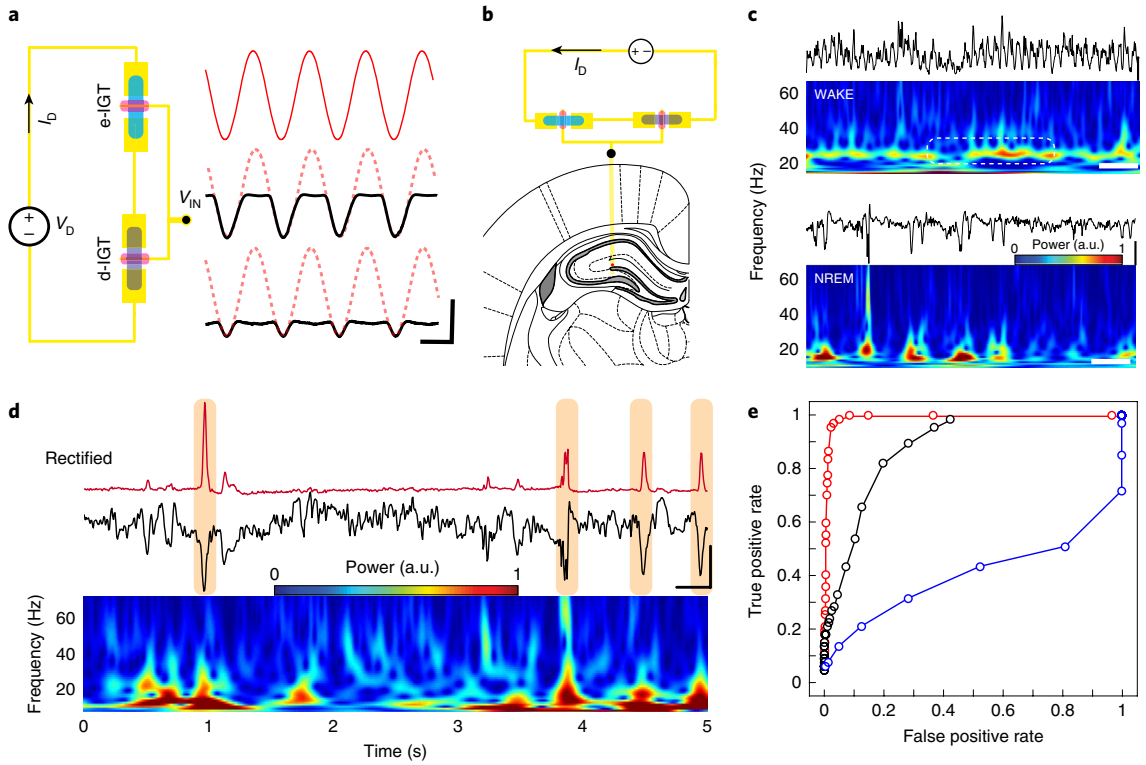

Fig. 6 | E-IGTs in combination with d-IGTs enable real-time non-linear signal rectification for the accurate detection of epileptic discharges in vivo. a, Schematic of a non-linear signal rectification circuit composed of a d-IGT and an e-IGT (left). Non-linearity of the IGT-based circuit output is accomplished by varying the geometry of the d-IGT relative to the e-IGT; a 1 Hz sine wave input provided to the IGT-based circuitry (top red trace) results in thresholding at 0 V when the d-IGT and e-IGT have equivalent geometries (middle black trace), but thresholding at negative voltages when the d-IGT is smaller than the e-IGT (lower black trace). Scale bar, 500 ms, 200 μA; note that the IGT-based circuit output is not to scale relative to the input trace, for visualization purposes. **b**, Anatomical schematic of a coronal slice of rat brain demonstrating the source of the neural recording in the hippocampus (red dot) with the circuit diagram for IGT-based real-time detection. **c**, Sample raw traces and accompanying spectrograms of neural signals recorded using an e-IGT implanted in a freely moving rat during wakefulness (top; scale bar, 500 nA, 500 ms) and NREM sleep (bottom; scale bar, 1 μA, 500 ms). Prominent theta band activity is present during the rat's locomotion (white dashed box). Warmer colours represent a higher relative power in arbitrary units. **d**, The IGT-based non-linear rectifier shown in **a** provides high signal-to-noise real-time detection of epileptic discharges. Sample raw trace (black; scale bar, 1 μA, 500 ms) and accompanying spectrogram reveal several epileptic discharges (orange boxes) that are transformed into easily detectable peaks by the IGT-based circuit (red). Warmer colours represent a higher relative power in arbitrary units. **e**, Receiver operating curves demonstrating the superior detection of epileptic discharges using the IGT-based circuit (red; area under curve = 0.96) compared with traditional detection approaches based on bandpass filtered power thresholding (black; area under curve = 0.62) and amplitude thresholding (blue; area under curve = 0.43; n = 167 interictal epileptiform discharges (IEDs)).

reservoirs within the e-IGT channel. Thus, the e-IGT architecture can be paired with high-mobility conducting polymers to further boost the speed of ion-based transistors. E-IGTs concurrently exhibit high transconductance and speed, resulting in a measure of the gain–bandwidth product several orders of magnitude above that of other ion-based transistors. We demonstrated the use of e-IGTs in a wide range of neurophysiological applications, including EMG, ECG, intracranial encephalography and action potential (AP) recording. These devices were stable in physiological environments, acquiring a high-quality signal over two weeks of implantation in a freely moving rodent. In all cases, signals acquired by e-IGTs had a high SNR and spatiotemporal resolution, comparable with the quality of signals generated using conventional electrodes with silicon-based amplifiers. However, e-IGTs bring key advantages compared with such systems. Amplification is local and does not require an external amplifier, allowing for the miniaturization and conformability of sensors. E-IGTs can be combined with d-IGTs to create integrated circuits that can perform disease-relevant local processing of neurophysiologic signals.

Furthermore, e-IGTs are composed of only biocompatible and commercially available materials that do not require encapsulation in biological environments and are not impaired by exposure to water or ions. The composite material of the channel can be reproducibly manufactured in large quantities and is solution processible, making it more accessible in a broad range of fabrication processes. E-IGTs are flexible and compatible with integration into a wide variety of conformable plastic substrates and have a low leakage current, permitting the fabrication of efficient integrated circuits. Sensing applications that require the sparse detection of analyte over long periods of time would benefit from the application of e-IGTs because a transistor that is normally OFF does not consume extensive power. Overall, we have shown that e-IGTs can serve as reliable components for bioelectronic devices, with the potential to improve our ability to transduce and modulate physiologic signals. E-IGTs are also suitable for translation to use in humans, offering a safe, reliable and high-performance building block for chronically implanted bioelectronics.

Online content

Any methods, additional references, Nature Research reporting summaries, source data, extended data, supplementary information, acknowledgements, peer review information; details of author

contributions and competing interests; and statements of data and code availability are available at https://doi.org/10.1038/s41563-020-0638-3.

Received: 10 August 2019; Accepted: 12 February 2020;
Published online: 16 March 2020

References

1. Chen, R., Canales, A. & Anikeeva, P. Neural recording and modulation technologies. *Nat. Rev. Mater.* **2**, 1–16 (2017).
2. Jeong, J. W. et al. Soft materials in neuroengineering for hard problems in neuroscience. *Neuron* **86**, 175–186 (2015).
3. Someya, T., Bao, Z. & Malliaras, G. G. The rise of plastic bioelectronics. *Nature* **540**, 379–385 (2016).
4. Spyropoulos, G. D., Gelinas, J. N. & Khodagholy, D. Internal ion-gated organic electrochemical transistor: a building block for integrated bioelectronics. *Sci. Adv.* **5**, eaau7378 (2019).
5. Fang, H. et al. Ultrathin, transferred layers of thermally grown silicon dioxide as biofluid barriers for biointegrated flexible electronic systems. *Proc. Natl Acad. Sci. USA* **113**, 11682–11687 (2016).
6. Kim, D.-H. et al. Stretchable and foldable silicon integrated circuits. *Nature* **320**, 507–511 (2008).
7. Cho, J. H. H. et al. High-capacitance ion gel gate dielectrics with faster polarization response times for organic thin film transistors. *Adv. Mater.* **20**, 686–690 (2008).
8. Kim, S. H. et al. Electrolyte-gated transistors for organic and printed electronics. *Adv. Mater.* **25**, 1822–1846 (2013).
9. Panzer, M. J. & Frisbie, C. D. Polymer electrolyte-gated organic field-effect transistors: low-voltage, high-current switches for organic electronics and testbeds for probing electrical transport at high charge carrier density. *J. Am. Chem. Soc.* **129**, 6599–6607 (2007).
10. Zare Bidoky, F. et al. Sub-3 V ZnO electrolyte-gated transistors and circuits with screen-printed and photo-crosslinked ion gel gate dielectrics: new routes to improved performance. *Adv. Funct. Mater.* https://doi.org/10.1002/adfm.201902028 (2019).
11. Song, E. et al. Flexible electronic/optoelectronic microsystems with scalable designs for chronic biointegration. *Proc. Natl Acad. Sci. USA* **116**, 15398–15406 (2019).
12. Rivnay, J. et al. Organic electrochemical transistors. *Nat. Rev. Mater.* **3**, 17086 (2018).
13. Giovannitti, A. et al. Controlling the mode of operation of organic transistors through side-chain engineering. *Proc. Natl Acad. Sci. USA* **113**, 12017–12022 (2016).
14. Nielsen, C. B. et al. Molecular design of semiconducting polymers for high-performance organic electrochemical transistors. *J. Am. Chem. Soc.* **138**, 10252–10259 (2016).
15. Schmode, P. et al. High-performance organic electrochemical transistors based on conjugated polyelectrolyte copolymers. *Chem. Mater.* **31**, 5286–5295 (2019).
16. Bernards, D. A. & Malliaras, G. G. Steady-state and transient behavior of organic electrochemical transistors. *Adv. Funct. Mater.* **17**, 3538–3544 (2007).
17. Stavrinidou, E. et al. Direct measurement of ion mobility in a conducting polymer. *Adv. Mater.* **25**, 4488–4493 (2013).
18. Khodagholy, D. et al. High speed and high density organic electrochemical transistor arrays. *Appl. Phys. Lett.* **99**, 163304 (2011).
19. Crispin, X. et al. The origin of the high conductivity of poly(3,4-ethylenedioxythiophene)–poly(styrenesulfonate) (PEDOT:PSS) plastic electrodes. *Chem. Mater.* **18**, 4354–4360 (2006).
20. Spyropoulos, G. D. et al. Organic and perovskite solar modules innovated by adhesive top electrode and depth-resolved laser patterning. *Energy Environ. Sci.* **9**, 2302–2313 (2016).
21. Zhou, Y. et al. A universal method to produce low–work function electrodes for organic electronics. *Org. Electron.* **873**, 327–332 (2012).
22. Lin, Z. et al. A work-function tunable polyelectrolyte complex (PEI:PSS) as a cathode interfacial layer for inverted organic solar cells. *J. Mater. Chem. A* **2**, 7788–7794 (2014).
23. Xuan, Y., Sandberg, M., Berggren, M. & Crispin, X. An all-polymer-air PEDOT battery. *Org. Electron. Phys. Mater. Appl.* **13**, 632–637 (2012).
24. Van de Burgt, Y. et al. A non-volatile organic electrochemical device as a low-voltage artificial synapse for neuromorphic computing. *Nat. Mater.* **16**, 414–418 (2017).
25. Zozoulenko, I. et al. Polarons, bipolarons, and absorption spectroscopy of PEDOT. *ACS Appl. Polym. Mater.* **1**, 83–94 (2019).
26. Ravi Kumar, M. N. V. A review of chitin and chitosan applications. *React. Funct. Polym.* **46**, 1–27 (2000).
27. Jiang, H. L. et al. Chitosan-graft-polyethylenimine as a gene carrier. *J. Control. Release* **117**, 273–280 (2007).
28. Khodagholy, D. et al. In vivo recordings of brain activity using organic transistors. *Nat. Commun.* **4**, 1575 (2013).
29. Khodagholy, D. et al. High transconductance organic electrochemical transistors. *Nat. Commun.* **4**, 2133 (2013).
30. Rivnay, J. et al. High-performance transistors for bioelectronics through tuning of channel thickness. *Sci. Adv.* 1 e1400251 (2015).
31. Inal, S., Malliaras, G. G. & Rivnay, J. Benchmarking organic mixed conductors for transistors. *Nat. Commun.* **8**, 1767 (2017).
32. Khodagholy, D. et al. NeuroGrid: recording action potentials from the surface of the brain. *Nat. Neurosci.* **18**, 310–315 (2015).
33. Krook-Magnuson, E., Gelinas, J. N., Soltesz, I. & Buzsáki, G. Neuroelectronics and biooptics: closed-loop technologies in neurological disorders. *JAMA Neurol.* **72**, 823–829 (2015).
34. Choi, H. H., Cho, K., Frisbie, C. D., Sirringhaus, H. & Podzorov, V. Critical assessment of charge mobility extraction in FETs. *Nat. Mater.* **17**, 2–7 (2018).
35. Rivnay, J. et al. Structural control of mixed ionic and electronic transport in conducting polymers. *Nat. Commun.* **7**, 11287 (2016).
36. Podzorov, V. Organic single crystals: addressing the fundamentals of organic electronics. *MRS Bull.* **38**, 15–24 (2013).
37. Crone, B. et al. Large-scale complementary integrated circuits based on organic transistors. *Nature* **403**, 521 (2000).
38. Kim, Y. et al. A bioinspired flexible organic artificial afferent nerve. *Science* **360**, 998–1003 (2018).
39. Sessolo, M. et al. Easy-to-fabricate conducting polymer microelectrode arrays. *Adv. Mater.* **25**, 2135–2139 (2013).
40. Khodagholy, D., Gelinas, J. N. & Buzsáki, G. Learning-enhanced coupling between ripple oscillations in association cortices and hippocampus. *Science* **372**, 369–372 (2017).
41. Peyrache, A., Battaglia, F. P. & Destexhe, A. Inhibition recruitment in prefrontal cortex during sleep spindles and gating of hippocampal inputs. *Proc. Natl Acad. Sci. USA* **108**, 17207–17212 (2011).
42. Khan, F., Tare, R. S., Oreffo, R. O. C. & Bradley, M. Versatile biocompatible polymer hydrogels: scaffolds for cell growth. *Angew. Chem. Int. Ed.* **48**, 978–982 (2009).
43. Buzsaki, G. Hippocampal sharp wave-ripple: a cognitive biomarker for episodic memory and planning. *Hippocampus* **25**, 1073–1188 (2015).
44. Morrell, M. J. Responsive cortical stimulation for the treatment of medically intractable partial epilepsy. *Neurology* **77**, 1295–1304 (2011).
45. González Otárula, K. A., Mikhaeil-Demo, Y., Bachman, E. M., Balaguera, P. & Schuele, S. Automated seizure detection accuracy for ambulatory EEG recordings. *Neurology* **92**, e1540–e1546 (2019).
46. Buzsáki, G., Anastassiou, C. A. & Koch, C. The origin of extracellular fields and currents—EEG, ECoG, LFP and spikes. *Nat. Rev. Neurosci.* **13**, 407–420 (2012).
47. Gelinas, J. N., Khodagholy, D., Thesen, T., Devinsky, O. & Buzsáki, G. Interictal epileptiform discharges induce hippocampal–cortical coupling in temporal lobe epilepsy. *Nat. Med.* **22**, 641–648 (2016).
48. Inal, S. et al. A high transconductance accumulation mode electrochemical transistor. *Adv. Mater.* **26**, 7450–7455 (2014).
49. Viventi, J. et al. Flexible, foldable, actively multiplexed, high-density electrode array for mapping brain activity in vivo. *Nat. Neurosci.* **14**, 1599–1605 (2011).
50. Zeglio, E. et al. Conjugated polyelectrolyte blends for electrochromic and electrochemical transistor devices. *Chem. Mater.* **27**, 6385–6393 (2015).

Publisher's note Springer Nature remains neutral with regard to jurisdictional claims in published maps and institutional affiliations.

© The Author(s), under exclusive licence to Springer Nature Limited 2020

Methods

Material preparation. PEDOT:PSS (Clevios PH1000) was purchased from Heraeus. D-sorbitol (≥99.5%; BioUltra), chitosan (low molecular weight), (3-glycidyloxypropyl)trimethoxysilane (GOPS), 4-dodecyl benzene sulfonic acid (DBSA), 3-(trimethoxysilyl)propyl methacrylate (A-174 silane), branched PEI and acetic acid were purchased from Sigma-Aldrich. Micro-90 concentrated cleaning solution was purchased from Special Coating Services. AZnLOF2020 (negative photoresist), AZ9260 (positive photoresist), AZ 400K and AZ 300MIF (metal ion free) developers were acquired from MicroChemicals, Merck. To create the transistor channel, a mixture of PEDOT:PSS aqueous dispersion and D-sorbitol (40 wt%) was prepared and mixed with GOPS (1 wt%) and DBSA (0.1 wt%). PEI (1 wt%) was diluted in deionized water (1:10). Chitosan (0.5 wt%) was diluted in deionized water and mixed with acetic acid (6 wt%).

Device fabrication. A 1.2-μm-thick parylene C layer was coated on quartz wafers (100 mm outer diameter (O.D.), thickness of 1 mm) using an SCS Labcoater 2. Metal electrodes and interconnects were patterned through a metal lift-off process. AZnLOF2020 photoresist was spin-coated at 3,000 r.p.m. on the substrate, baked at 105 °C for 90 s, exposed to ultraviolet light using a Suss MA6 Mask Aligner and developed with AZ 300MIF developer. A 10-nm-thick Ti adhesion layer, followed by a 150-nm-thick Au layer, was deposited (Angstrom EvoVac Multi-Process) and patterned by soaking the substrate in a bath of resist remover. A second layer of parylene C (insulation layer), followed by an additional sacrificial layer of parylene C (for the subsequent peel-off process) were deposited. The adhesion between the first and the second layer of parylene C was enhanced by the addition of 3-(trimethoxysilyl)propyl methacrylate (A-174 silane) during chemical vapour deposition while an anti-adhesion agent (5 wt% Micro-90 diluted in deionized water) reduced the adhesion between the second and third layers. The stacked layers were patterned with a layer of AZ9260 positive photoresist and dry etched with a plasma-reactive ion-etching process (Oxford Plasmalab 80; 180 W, 50 sccm O_2 and 2 sccm SF_6) to shape the transistor channel area and electrical contact pads. Specifically, AZ9260 was spin-coated at 5,000 r.p.m., baked at 115 °C for 90 s, exposed using a Suss MA6 Mask Aligner and developed with AZ400K developer (1:4 with deionized water). To guard the first layer of parylene from being over-etched, an extra layer of AZnLOF2020 (3,000 r.p.m.) was added between the metal layer and the silane-treated parylene. The transistor channels were realized by spin coating PEDOT:PSS and a layer of PEI (500 r.p.m.) and patterned by peeling off the last parylene layer. All IGTs and circuits were fabricated using chitosan as the ion membrane with the exception of the devices presented in Supplementary Fig. 2. OECTs were fabricated based on previously described methods[28,29].

Electrical characterization. Current–voltage characteristics were measured with a Keysight B2902A Precision Source/Measurement Unit using two channels. On the first channel supplied V_D and measured I_D while the second channel provided V_G. The OECTs were measured using Ag/AgCl as gate electrodes immersed in ×1 PBS. Temporal responses for IGTs and OECTs were recorded with a Keysight InfiniiVision EDUX1002. Gate voltage pulses were supplied by a function generator (Keysight 33500B Series), whereas drain voltage was provided by a source measurement unit (Keysight B2902A). The drain current was derived by measuring the voltage fluctuations across a 100 Ω resistor in series with the IGT channel. The resulting drain current curve was fitted with a single exponential decay equation to extract the time constant of the transistors.

Animal surgical procedure. All the animal experiments were approved by the Institutional Animal Care and Use Committee of Columbia University. The implantations were carried out on the cortex of male Long Evans rats (250–350 g; 8–11 weeks of age) that had no previous experimentation. The animals were housed in a regular 12 h/12 h light/dark cycle. Prior to the surgical procedure the rats were housed in pairs, and they were separated post-implantation. Animals were anesthetized with 2% isoflurane and maintained under anaesthesia with 0.75–1% isoflurane during the intracranial implantation surgery. Methylprednisolone (30 mg kg^{-1}) was administered to minimize cortical oedema intra-operatively. Two #000-gauge stainless-steel screws were implanted in the cerebellum and used as gate electrodes. A craniotomy (2 × 3 mm^2) was performed on the right hemisphere (anteroposterior = 3.0 mm, mediolateral = 3.0 mm), and the cortical surface was exposed upon removal of the dura mater. The e-IGTs were placed on the cortical surface, and the craniotomy was covered with medical silicone. After a post-operative recovery period, recordings of the electrophysiological activity from the animals were performed while they moved freely in their home cages. For the implantation of e-IGTs into deep cortical layers, the procedures as described above were performed to generate a craniotomy and reference/ground electrodes. The implantable e-IGT probe was placed on the surface of the cortex and inserted to a depth of 1.5 mm using a 50 μm tungsten wire. The tungsten wire was anchored to the parylene substrate through a microfabricated hole pierced at the front end of the e-IGT probe. Recordings of LFPs and APs occurred intra-operatively.

Animal kindling procedure. To induce IEDs, the rats underwent a hippocampal commissure electrical stimulation protocol using a bipolar stimulator (a pair of 50 μm tungsten wires with a 500 μm dorsoventral tip separation) implanted at the hippocampal commissure (−0.5 anteroposterior (AP), 0.8 mediolateral (ML), −4.2 dorsoventral (DV)). During the first kindling session, a minimal current amount is used (25 μA), and the animal's behaviour and neurophysiological recordings are analysed for seizure activity. The amount of current is increased in small (25 μA) increments to determine the minimal amount needed to evoke a seizure that lasts at least 10 s. This amount of current is used for all future kindling sessions. Seizures are evoked by the delivery of 1 train of electrical stimulation, and the seizure duration ranges from 10 s to 3 min. No seizures occur in the absence of electrical stimulation applied by the experimenter. There is no pain associated with the electrical stimulation or seizure. IEDs typically emerge after 4–5 days of kindling.

EMG and ECG recording. ECG and EMG recordings were performed on healthy volunteers. Before each recording, the skin at the recording sites was cleaned using soap and 50% v/v isopropyl alcohol. For the ECG recordings, the e-IGT probe was placed on the skin over the left anterior chest. For the EMG recordings, the e-IGT probe was placed on the skin over the left biceps muscle. In both cases, the reference (gate) electrode was an adhesive electrode placed on the skin over the right wrist (3M Red Dot). Signals were acquired by sampling at 1 kHz, using a custom board incorporating a transimpedance amplifier and visualized in real time with the Keysight InfiniiVision EDUX1002 oscilloscope. Data were stored for analysis in a 16-bit format and analysed with MATLAB (MathWorks). Signals were notch filtered (60 Hz) before further processing.

Local field potential and spike analysis. We used custom MATLAB software to score behaviour into NREM sleep, REM sleep and waking epochs based on spectral features and an onboard accelerometer. Spectral analyses were generated using wavelet (Gabor), and cross-frequency coupling was performed as established previously[40]. An amplitude-threshold method was used to detect spikes from bandpass filtered data (0.25–2.5 kHz), and spike waveforms were retrieved from wideband files.

Reporting Summary. Further information on research design is available in the Nature Research Reporting Summary linked to this article.

Data availability

All data needed to evaluate the conclusions in the paper are present in the paper and/or the Supplementary Information. All source files and experimental data are freely and publicly available at www.dion.ee.columbia.edu. Additional data related to this paper may be requested from the authors.

Acknowledgements

This work was supported by Columbia University, School of Engineering and Applied Science as well as Columbia University Medical Center, Department of Neurology and Institute for Genomic Medicine. The device fabrication was performed at Columbia Nano-Initiative (CNI) and at Cornell NanoScale Facility (CNF), a member of the National Nanotechnology Coordinated Infrastructure (NNCI), which is supported by the National Science Foundation (Grant ECCS-1542081). G.D.S. is supported through the Human Frontiers Postdoctoral Fellowship Program. This work was supported by an NIH grant (1U01NS108923-01), NSF CAREER award (1944415), CURE Taking Flight Award, Columbia School of Engineering. We thank M. Gonzalez, J. Yu, J. Vichiconti, Y. Borisenkov, P. Chow, C. Belfer, N. Ariel-Sternberg (CNI) and all Khodagholy and Gelinas laboratory members for their support.

Author contributions

D.K., J.N.G. and C.C. conceived the project. C.C., D.K., G.D.S. and P.J. designed, developed, fabricated and characterized the materials and devices. C.C. and G.D.S. fabricated the neural probes for the rodent and human recordings. C.C. and G.D.S. performed the ECG and EMG recordings. D.K., C.C., J.J.F. and J.N.G. performed the electrophysiology in vivo rodent experiments and analysis. All authors contributed to writing the paper.

Competing interests

The authors declare no competing interests.

Additional information

Supplementary information is available for this paper at https://doi.org/10.1038/s41563-020-0638-3.

Correspondence and requests for materials should be addressed to J.N.G. or D.K.

Reprints and permissions information is available at www.nature.com/reprints.

nature research

Corresponding author(s): Dion Khodagholy
Jennifer Gelinas

Last updated by author(s): Jan 21, 2020

Reporting Summary

Nature Research wishes to improve the reproducibility of the work that we publish. This form provides structure for consistency and transparency in reporting. For further information on Nature Research policies, see Authors & Referees and the Editorial Policy Checklist.

Statistics

For all statistical analyses, confirm that the following items are present in the figure legend, table legend, main text, or Methods section.

n/a	Confirmed	
☐	☒	The exact sample size (*n*) for each experimental group/condition, given as a discrete number and unit of measurement
☐	☒	A statement on whether measurements were taken from distinct samples or whether the same sample was measured repeatedly
☒	☐	The statistical test(s) used AND whether they are one- or two-sided *Only common tests should be described solely by name; describe more complex techniques in the Methods section.*
☒	☐	A description of all covariates tested
☒	☐	A description of any assumptions or corrections, such as tests of normality and adjustment for multiple comparisons
☒	☐	A full description of the statistical parameters including central tendency (e.g. means) or other basic estimates (e.g. regression coefficient) AND variation (e.g. standard deviation) or associated estimates of uncertainty (e.g. confidence intervals)
☒	☐	For null hypothesis testing, the test statistic (e.g. *F*, *t*, *r*) with confidence intervals, effect sizes, degrees of freedom and *P* value noted *Give P values as exact values whenever suitable.*
☒	☐	For Bayesian analysis, information on the choice of priors and Markov chain Monte Carlo settings
☒	☐	For hierarchical and complex designs, identification of the appropriate level for tests and full reporting of outcomes
☒	☐	Estimates of effect sizes (e.g. Cohen's *d*, Pearson's *r*), indicating how they were calculated

Our web collection on statistics for biologists contains articles on many of the points above.

Software and code

Policy information about availability of computer code

Data collection	Intan RHD2000 V1.5.3 Keysight quick IV 4.1.1821.3680 Keysight InfiniiVision EDUX1002
Data analysis	MATLAB 2018b Neuroscope v1.0

For manuscripts utilizing custom algorithms or software that are central to the research but not yet described in published literature, software must be made available to editors/reviewers. We strongly encourage code deposition in a community repository (e.g. GitHub). See the Nature Research guidelines for submitting code & software for further information.

Data

Policy information about availability of data

All manuscripts must include a data availability statement. This statement should provide the following information, where applicable:

- Accession codes, unique identifiers, or web links for publicly available datasets
- A list of figures that have associated raw data
- A description of any restrictions on data availability

All data and computer code needed to evaluate the conclusions in the paper are present in the paper and/or the Supplementary Materials. Additional data related to this paper may be requested from the authors.

Field-specific reporting

Please select the one below that is the best fit for your research. If you are not sure, read the appropriate sections before making your selection.

☒ Life sciences ☐ Behavioural & social sciences ☐ Ecological, evolutionary & environmental sciences

For a reference copy of the document with all sections, see nature.com/documents/nr-reporting-summary-flat.pdf

Life sciences study design

All studies must disclose on these points even when the disclosure is negative.

Sample size	n= 4 rats
Data exclusions	No data excluded
Replication	Experiments were replicated with multiple independent devices and measurements
Randomization	No randomization was performed - not applicable to this study design
Blinding	No blinding was performed - not applicable to this study design

Reporting for specific materials, systems and methods

We require information from authors about some types of materials, experimental systems and methods used in many studies. Here, indicate whether each material, system or method listed is relevant to your study. If you are not sure if a list item applies to your research, read the appropriate section before selecting a response.

Materials & experimental systems

n/a	Involved in the study
☒	☐ Antibodies
☒	☐ Eukaryotic cell lines
☒	☐ Palaeontology
☐	☒ Animals and other organisms
☒	☐ Human research participants
☒	☐ Clinical data

Methods

n/a	Involved in the study
☒	☐ ChIP-seq
☒	☐ Flow cytometry
☒	☐ MRI-based neuroimaging

Animals and other organisms

Policy information about studies involving animals; ARRIVE guidelines recommended for reporting animal research

Laboratory animals	Long Evans rats, male, 250-300g
Wild animals	The study did not involve wild animals
Field-collected samples	The study did not involve field-collected samples
Ethics oversight	IACUC - Columbia University

Note that full information on the approval of the study protocol must also be provided in the manuscript.